

## RESEARCH ARTICLE

10.1002/2013JG002522

## Key Points:

- An integrated ocean-atmosphere-biology modeling system is developed
- Biothermal feedback to physics alters the ocean-atmosphere model results
- Biothermal feedback also enhances the simulated phytoplankton growth

## Correspondence to:

J. K. Jolliff,  
jolliff@nrlssc.navy.mil

## Citation:

Jolliff, J. K., and T. A. Smith (2014), Biological modulation of upper ocean physics: Simulating the biothermal feedback effect in Monterey Bay, California, *J. Geophys. Res. Biogeosci.*, 119, doi:10.1002/2013JG002522.

Received 27 SEP 2013

Accepted 28 MAR 2014

Accepted article online 8 APR 2014

## Biological modulation of upper ocean physics: Simulating the biothermal feedback effect in Monterey Bay, California

Jason K. Jolliff<sup>1</sup> and Travis A. Smith<sup>1</sup><sup>1</sup>Naval Research Laboratory, Stennis Space Center, Mississippi, USA

**Abstract** Marine phytoplankton and associated organic materials absorb a substantial quantity of solar shortwave energy penetrating the upper ocean. Most of this absorbed energy is lost as heat and thereby contributes to the warming of near-surface waters. Here we examine this biothermal feedback effect on upper ocean physics and air-sea energy exchange using a fully integrated ocean-atmosphere-biological modeling system. Our model simulations show that a local phytoplankton bloom may impact upper ocean physics in such a way as to promote the spatiotemporal persistence of the bloom itself within a semi-enclosed coastal embayment. This is accomplished primarily via enhanced thermal stratification that promotes vertical stability and more efficient utilization of macronutrients. Modulations of wind stress patterns due to perturbations in the local surface pressure gradients also arise as a result of the simulated biothermal warming of surface waters. The model evidence suggests that the observed persistence of phytoplankton blooms in the northern Monterey Bay, California, may be enhanced by similar synergistic interactions between ocean biology and physics.

### 1. Introduction

A fundamental concept in biological oceanography is that the physical processes of the oceans largely determine the spatiotemporal variability of phytoplankton abundance and productivity. For example, the wind-driven coastal divergence of surface waters along the eastern ocean margins results in the upwelling of nutrient-rich deeper waters that stimulate microalgal growth [Chavez and Messié, 2009; Walsh, 1988]. The main features of global phytoplankton abundance evident in synoptic satellite data may indeed be broadly explained in this context of geophysical forcing [see Longhurst, 1998].

However, the abundance of marine phytoplankton belies the inefficiency of photosynthesis as a photochemical process: most of the light energy absorbed by algal pigments is lost to the surrounding environment as heat [Morel, 1978; Bannister and Weidemann, 1984; Morel, 1988]. Accordingly, it has been theorized that marine phytoplankton have the potential capacity to modulate the heating of the upper ocean due to the optical properties of microalgal pigments [Lewis et al., 1983; Morel, 1988]. Furthermore, the high turnover rate of algal biomass (~ 2 days [Falkowski, 1994]) generates more temporally persistent nonliving organic matter that absorbs substantial quantities of solar energy in the surface ocean [Bricaud et al., 1981]. Thus, the aggregate biothermal impact of phytoplankton and associated organic constituents upon the heat budget of the upper ocean is not negligible [Morel and Antoine, 1994].

Quantitatively resolving the biothermal feedback effect upon oceanographic processes is nonetheless difficult. An observational study would ideally require a control so that identical atmospheric and physical oceanographic conditions may be experienced with and without the additional optical attenuation provided by phytoplankton and associated organic constituents. Given that this approach is not feasible, most of the progress toward understanding the biothermal impacts has been accomplished via ocean models where such an experiment may be performed within the simulations [Anderson et al., 2007; Cahill et al., 2008; Manizza et al., 2008; Oschlies, 2004; Rochford et al., 2001; Sweeney et al., 2003; Wu et al., 2007]. More recently, two-way coupled ocean-atmosphere numerical models suggest that this biothermal effect is significant on global and climatic scales [Patara et al., 2012] as well as locally and on much shorter timescales [Jolliff et al., 2012a]. Two-way coupled ocean-atmosphere modeling systems better approximate the air-sea exchange of thermal energy as constrained by conservation; however, continuing dynamical impacts back upon the surface biota cannot be assessed without an additional biological model. In this paper, this deficiency is addressed by integrating a biological model into a numerical ocean-atmosphere modeling system. This allows for not merely an

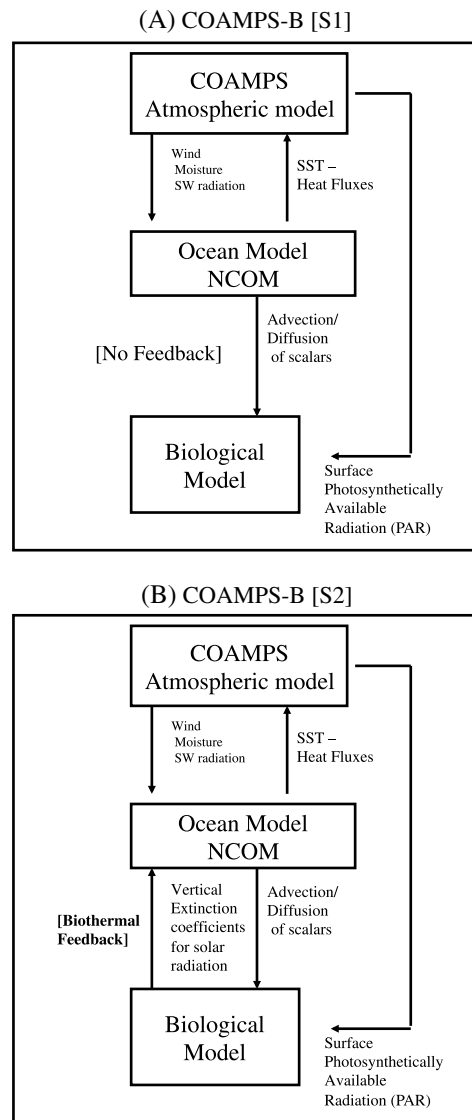


**Figure 1.** Schematic of the COAMPS-B modeling system. Arrows and text summarize the communication between the modeling components. (a) The model schematic for COAMPS-B with the biothermal feedback disabled (S1). (b) Biothermal feedback as the transfer of vertical optical attenuation coefficients the physical model uses to determine the penetration of solar shortwave radiation into the surface ocean. This model (Figure 1b) is used for simulation 2 (S2).

terms are provided back to the physical ocean model. Thus, changes in the biological state variables have the potential to impact the simulated thermodynamic upper ocean processes. The specific details of the biological model and its interface with the physical models are provided in Appendix A.

To isolate the potential impact of the biothermal feedback in the model, two simulations are performed: (S1) the feedback from the biology is disabled (Figure 1a); and (S2) the feedback from the biology to the physics is active (as in Figure 1b). In the former simulation (S1), the physical ocean model (NCOM) presumes a constant set of optical attenuation terms based on the work of Paulson and Simpson [1977]. These computations are an approximation of the Jerlov water types [Jerlov, 1976], and they are often used in physical ocean models [Kara et al., 2004; Rochford et al., 2001]. Whereas these terms may constitute a reasonable approach in some cases, the

assessment of how biothermal effects may impact the physics but also a further analysis of how these physical impacts may, in turn, impact the biology.

## 2. Methods

The Naval Research Laboratory (NRL) has developed a fully integrated ocean-atmosphere-biological numerical modeling system based on the Coupled Ocean-Atmosphere Mesoscale Prediction System (COAMPS®). COAMPS is a nested, relocatable, and two-way coupled ocean-atmosphere modeling system that is presently used for ocean-atmosphere forecasting by the U.S. Navy. The nonhydrostatic atmospheric COAMPS model component [Hodur, 1997] is the Navy's operational mesoscale meteorological forecasting system. The hydrostatic Navy Coastal Ocean Model (NCOM) [Barron et al., 2004] serves as the oceanic component of COAMPS. This modeling component was executed in data-assimilative mode via the Navy Coupled Ocean Data Assimilation system [Cummings, 2005] for a 1 month spin-up (beginning on 1 April 2008) and then in non-data-assimilative (or "free-run" mode) for the remaining 3 months of the simulation (ending 31 July 2008). The atmospheric and oceanic model coupling was designated via the uppermost oceanic model grid cell temperature and the lowest grid cell atmospheric model variables (temperature, humidity, wind velocity, pressure, and radiative fluxes). At a 6-min coupling interval, bulk fluxes of thermal energy exchange were calculated following the Coupled Ocean-Atmosphere Response, version 3, scheme [Fairall et al., 1996].

The integration of a four-component, nitrogen-based biological model into COAMPS (Figure 1) occurs first via the conventional means: biological state variables (phytoplankton biomass, nitrate nitrogen, ammonium nitrogen, and particulate detritus nitrogen) are physically forced by the advection and diffusion resolved by the ocean circulation model (NCOM). The physical ocean model, however, must also be informed about how to attenuate solar energy to meet its requirement for solar heating rate computations. The ocean biology model provides this information. Biological state variables are used to estimate the bio-optical attenuation, and these

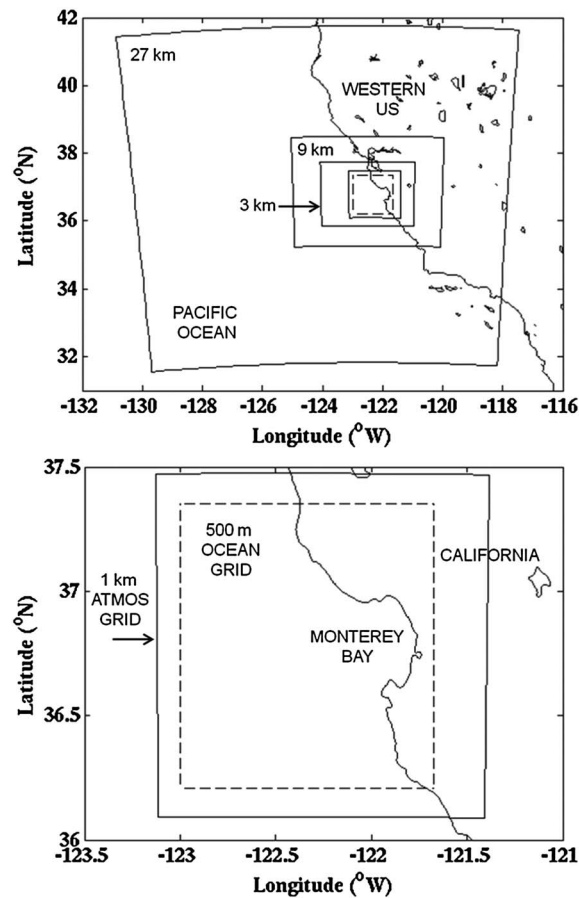


**Figure 2.** (a) The COAMPS atmospheric model nests beginning at 27 km horizontal resolution and scaling down to the inner nest of 3 km resolution over the Monterey Bay, California, area. (b) The innermost atmospheric nest (1 km) overlaid the inner ocean model nest (500 m horizontal resolution).

southern portion of the bay brings about a semicyclonic circulation within the bay [see *Ramp et al.*, 2005]. The intense surface currents (a surface “jet”) across the mouth of the bay prevent egress of the surface waters out its northwestern periphery. The Santa Cruz Mountains immediately to the north of this area effectively block the prevailing northwesterly winds. This combination of physical conditions sets up a relatively calm and retentive regime for the northeastern waters of Monterey Bay. Hence, this area is referred to as the “upwelling shadow” [Graham and Largier, 1997]. The retentive nature of the surface flow subjects these waters to elevated surface warming and enhanced biological productivity such that satellite detection of sea surface temperature (SST) and surface chlorophyll routinely depict elevated signals in northern Monterey Bay [e.g., *Ryan et al.*, 2010].

Herein COAMPS-B is used to simulate the physical and biological processes that occur in Monterey Bay’s upwelling shadow. The objective is to isolate the potential for biothermal effects to impact the physical and biological processes that occur within this semi-enclosed embayment. In section 4.1, the differences in the physical simulations are examined when biothermal effects are accounted for in the modeling system. In section 4.2, the potential for synergy between the interacting biological and physical fields are examined, and section 4.3 examines in situ data in light of these analyses. The in situ data were collected in Monterey Bay during June 2008 as part of an NRL field program; additional details may be found in *Jolliff et al.* [2012b].

## 4. Results

### 4.1. Biothermal Impact on the Simulated Physics

The differences between the simulations demonstrate the potential biothermal perturbation provided by the presence of phytoplankton in the surface ocean. For example, a longitudinal cross section through the

main point of criticism is that they are not dynamic, i.e., the optical attenuation terms are invariant and so they cannot mimic the dynamic spatiotemporal changes in ocean bio-optical properties that may occur in many coastal settings.

### 3. Study Site

The COAMPS-B (COAMPS with a Biological module) nested domain is established over Monterey Bay, California (herein “MB”; Figure 2). It is important to note that verification and validation of the COAMPS forecasting system may be found elsewhere [Doyle *et al.*, 2009; Eliassen *et al.*, 2005; Small *et al.*, 2012]. Here the focus is placed on the modeling system’s sensitivity to changes in the oceanic shortwave attenuation that arise as a result of the dynamic surface ocean phytoplankton variability that is simulated by an ocean biological model.

From March through November, the coastal region surrounding MB is subject to sustained northwesterly winds resulting in coastal upwelling. Periodic slackening of these upwelling winds are referenced as “relaxation” events [Breaker and Broenkow, 1994; Pennington and Chavez, 2000]. During upwelling winds, cold water filaments north and south of the bay arise from the coastal divergence and a strong equatorward flow of surface waters is often observed across the mouth of the bay.

Divergence of the southward flow toward the

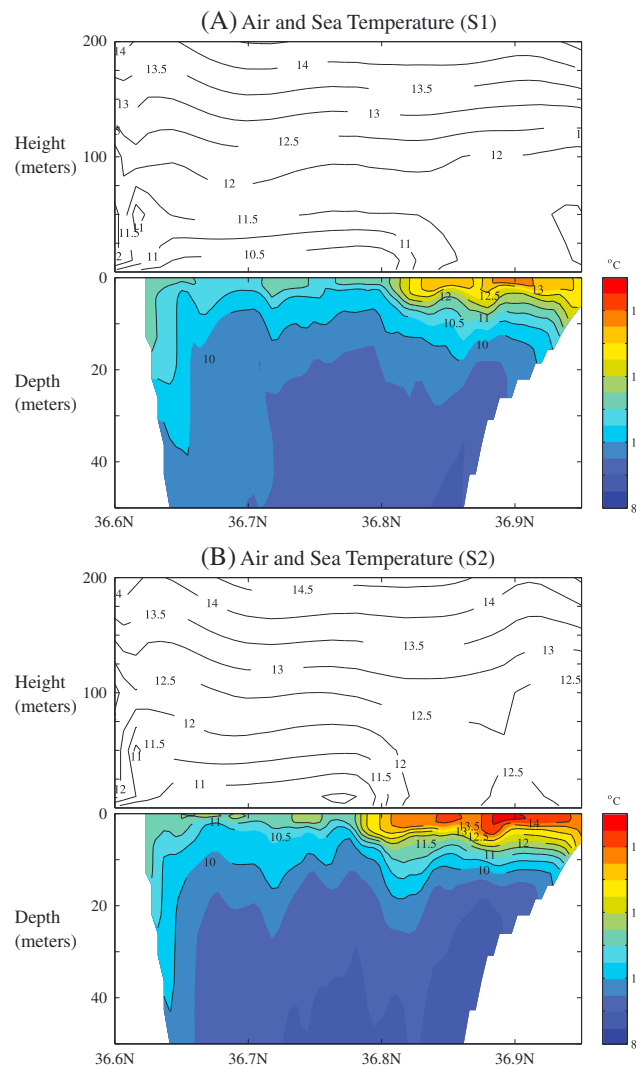


**Figure 3.** (a) A longitudinal cross section of the simulated (top) atmospheric temperatures and (bottom) ocean temperatures for simulation S1. (b) The same results for S2. Both results are from 14 June 2008 at 1200 GMT.

relaxation event reveal a substantial difference in surface warming (Figures 5a and 5b). This heating difference may also be shown by computing the spatially averaged SST in northern MB (north of 36.8°N and west of -122.1°W, as shown in Figures 5a and 5b) and calculating the difference between the respective simulation means at the hourly simulation output increment ( $S2 - S1$ ; Figure 5c). By 300 h into the June simulation, the mean SST differences begin to peak at  $\sim 1^\circ\text{C}$ . These temperature differences are transmitted to the lower atmosphere overlying the northern bay as a temperature difference also approaching  $\sim 1^\circ\text{C}$  (Figure 6a). This warmer air has a greater capacity to retain water vapor, and the simulated relative humidity is thereby reduced downward by as much as 8% (Figure 6b). This relative humidity decrease obscures the overall modest increase in total water vapor content for S2 (data not shown). This increased heat and moisture content in the lower atmosphere of S2 is principally due to the increase in latent heat flux resolved by the simulation. The spatially averaged latent heat flux differences peak as high as  $15 \text{ W m}^{-2}$  after 300 h (Figure 6c).

The simulated presence of phytoplankton warms the upper ocean, increases the upper ocean thermal stratification, and increases the temperature of the overlying lower atmosphere. These simulated effects are conspicuous during the wind relaxation periods when local effects prevail, as opposed to the dominant forcing of the regional-scale wind stress patterns. From an energy conservation point of view, the heat retentive capacity of the phytoplankton in the upper ocean effectively traps a greater amount of solar

COAMPS-B model results for the ocean and atmosphere (Figure 3) reveals an upper surface ocean ( $< 10 \text{ m}$ ) warming and enhanced thermal stratification in S2 that is not present in S1, particularly in the northern portion of the transect (north of 36.8°N). The simulations are two-way coupled between the atmospheric and oceanic model components. The biothermal perturbation present in the ocean is thereby transmitted to the simulated lower atmosphere. The lower atmosphere in the northern portion of the bay is as much as  $\sim 1^\circ\text{C}$  warmer in S2 (Figure 3).

These coupled ocean-atmosphere simulation results are very similar to what was reported in Jolliff *et al.* [2012a]. In the earlier work, satellite data rather than an integrated biological model determined the oceanic shortwave penetration depth. These simulations also suggest that the additional thermal energy retained by phytoplankton near the surface results in elevated turbulent heat flux transfers from the ocean to the atmosphere. These differences are acute during the relaxation periods of the prevailing northwesterly winds (Figure 4a), which were mimicked by the COAMPS atmospheric model component (Figure 4b) from approximately 13 to 15 June.

Differences in the mean SST fields immediately before (10–12 June) and during (13–15 June) the midmonth

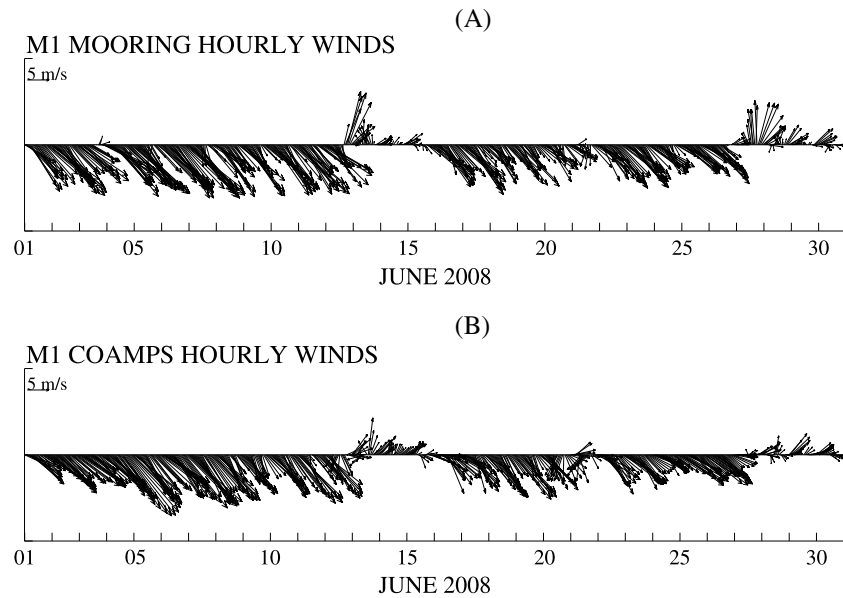


**Figure 4.** (a) Measured wind velocities ( $\text{m s}^{-1}$ ) at Monterey Bay Aquarium Research Institute (MBARI) mooring M1 from 1 to 30 June 2008; (b) the corresponding wind velocities from COAMPS.

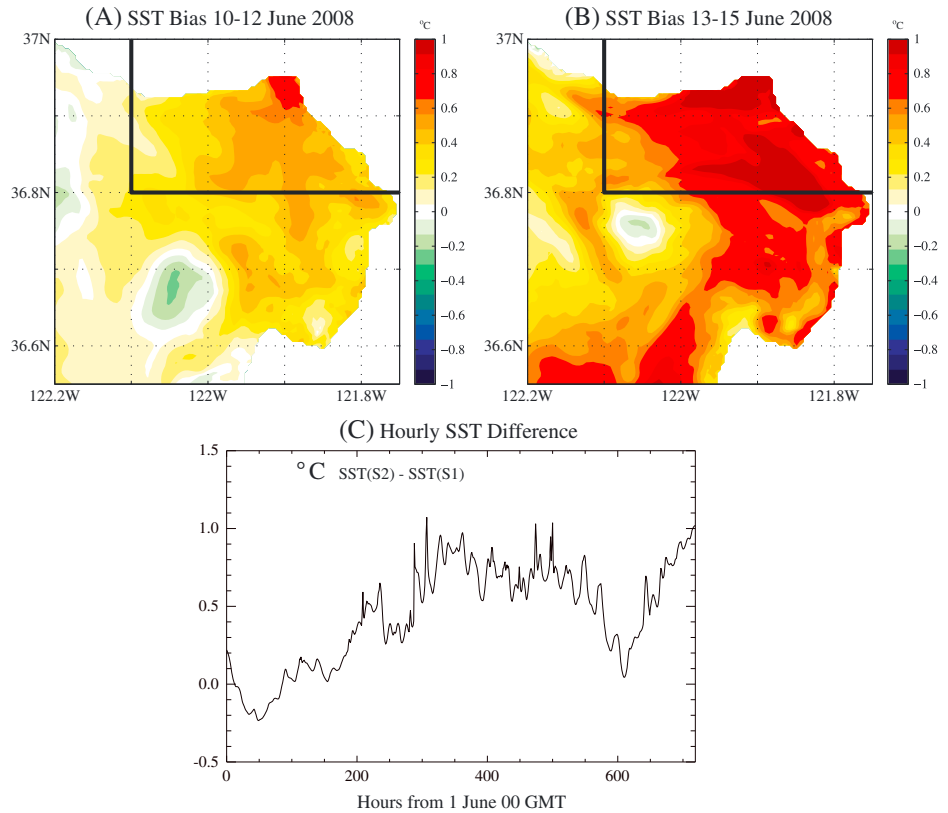


**Figure 5.** (a) The difference in the temporal means in SST ( $^{\circ}\text{C}$ ) between S2 and S1 for the period 10–12 June. (b) The difference in the temporal means in SST between S2 and S1 for the period 13–15 June. (c) The hourly difference in the mean SST fields ( $S2 - S1$ ) for June. The means are drawn from the area of northern MB indicated in Figures 5a and 5b.

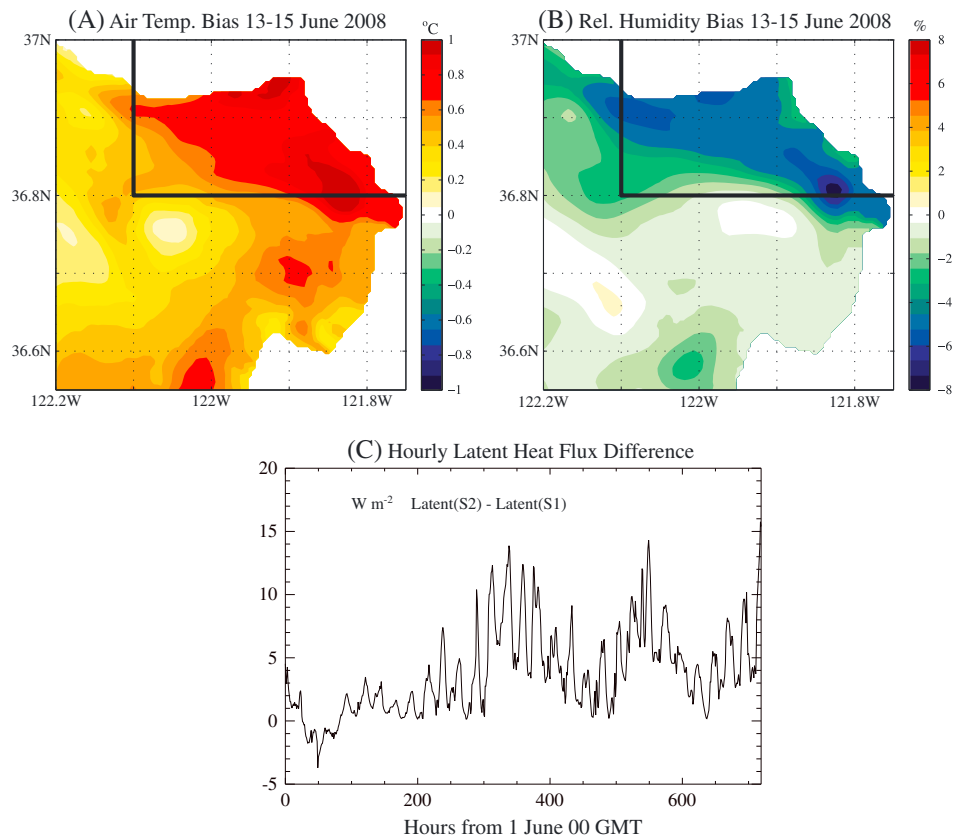


**Figure 6.** (a) The difference in the temporal means in 2 m air temperature ( $^{\circ}\text{C}$ ) between S2 and S1 for the period 13–15 June. (b) The difference in the temporal means in the relative humidity (%) between S2 and S1 for the period 13–15 June. (c) The hourly difference in the mean latent heat flux fields ( $\text{S2} - \text{S1}$ ;  $\text{W m}^{-2}$ ) for June. The means are drawn from the area of northern MB indicated in Figures 5a and 5b.

shortwave near the air-sea interface. This energy increase is readily fluxed back into the lower atmosphere. There are two additional simulated consequences to the biothermal perturbation resolved here: (1) the changes in fluid densities and energy fluxes appear to have some influence on simulated local wind patterns and upper ocean circulation during the wind relaxation period; and (2) the increased near-surface ocean stratification appears to amplify the surface biological productivity.

The first of these effects is minor but cannot be summarily dismissed as negligible. For example, the lower level heating and moisture increase in S2 introduces a  $\sim 0.04$  hPa lowering of sea level pressure over the northern bay (Figure 7a). Nonetheless, this modest decrease is enough of a local deviation in the zonal pressure gradient to comparatively accelerate the mean westerly component of the wind velocity by  $\sim 0.3 \text{ m s}^{-1}$  (Figure 7b). The simulated instantaneous wind velocity differences approach  $1.0 \text{ m s}^{-1}$  in the center of Monterey Bay on 14 June 2008.

The magnitude of the wind velocity differences is not large since the overall wind forcing is diminished during the relaxation period. The salient point is that during periods when local conditions within Monterey Bay dominate the physical dynamics, as when the regional wind patterns driven by the larger-scale pressure gradients are diminished, the air and sea planetary boundary layer circulation resolved by the two simulations become incoherent. For example, the S1 and S2 north/south surface water transports through the bay (through  $36.8^{\circ}\text{N}$ ) are highly correlated until the 13 June relaxation period when the transports become significantly out of phase (Figure 8, solid line). This episode corresponds to a mismatch in the simulated westerly wind stress magnitudes over the bay (Figure 8, thick line). The eddy kinetic energy of the surface currents (computed as  $[u^2 + v^2]/2$ ) is also diminished in S2 during the relaxation period (Figure 8, dashed line).

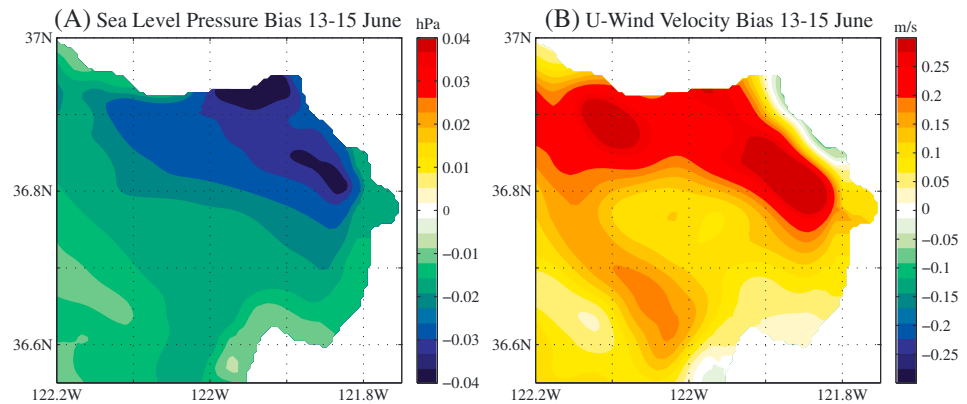


**Figure 7.** (a) The difference in the temporal means for sea level pressure (hPa) between S2 and S1 for the period 13–15 June. (b) The difference in the temporal means of the westerly component of the winds ( $\text{m s}^{-1}$ ) between S2 and S1 for the period 13–15 June.

**4.2. Synergy Between Biological and Physical Fields**

Simulated upper ocean chlorophyll distributions are spatially coherent to those of SST in the northern portion of MB during the wind relaxation regime (Figure 9). The amplification of both chlorophyll and SST from S1 to S2 suggests a synergy between the two variables. The most obvious mechanism is that the enhanced thermal stratification in S2 promotes enhanced phytoplankton growth near the surface, which in turn, promotes a further enhancement of thermal stratification via the biothermal feedback effect. The simulations quantify this potential synergy in northern MB as approximately  $0.8^\circ\text{C}$  in increased SST and  $2.9 \text{ mmol C m}^{-3}$  additional surface phytoplankton biomass on 14 June (1200 GMT). These are the differences in spatial simulation averages from northern MB; differences in average quantities are referred to herein as a “bias.” The biomass bias is particularly significant when examined in light of the S1 average biomass quantity, i.e., the ratio of the biomass bias  $[\text{mean}(S1) - \text{mean}(S2)]$  to the initial simulation mean  $[\text{mean}(S1)]$ . The biothermal effect increases the simulated surface biomass by 27%.

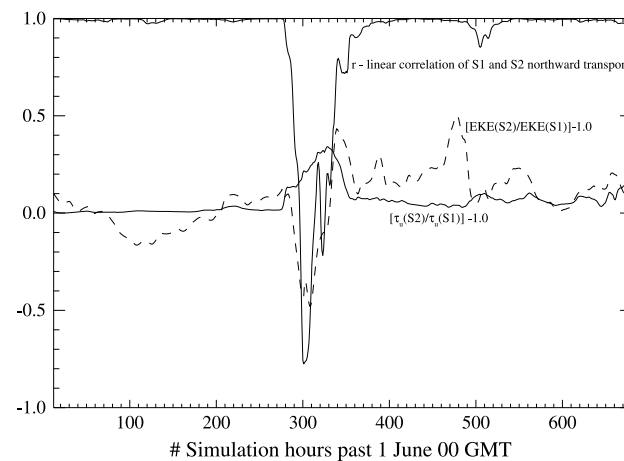


**Figure 8.** The linear correlation between north/south surface water transport ( $\text{m}^3 \text{ s}^{-1}$ ) to 10 m depth along  $36.8^\circ\text{N}$  from  $-122.1^\circ\text{W}$  to the coastal boundary is shown by the thin line. The thick line is the ratio of the S2 to S1 wind stress  $(\tau_u(S2)/\tau_u(S1) - 1.0)$ ; the dashed line is the ratio of surface current eddy kinetic energy EKE  $(\text{EKE}(S2)/\text{EKE}(S1) - 1.0)$ , where  $\text{EKE} = ((u^2 + v^2)/2)$ . EKE and  $\tau_u$  values were first smoothed with a running 24 h (24 point) average.

Thermal upper ocean stratification within northern MB, quantified as  $\Delta T$  from the surface to 22 m depth ( $\Delta T_{22}$ ), is biased upward by  $\sim 1^\circ\text{C}$  in S2 during the simulated wind relaxation period (Figure 10). SST and surface chlorophyll are similarly elevated (by an average of  $0.8^\circ\text{C}$  and  $0.7 \text{ mg chl m}^{-3}$ , respectively; Figure 10). The simulations do not feature variable carbon-to-chlorophyll ratios (see section A1); these differences in chlorophyll are directly forced by differences in simulated phytoplankton biomass.

Indeed, the relative simplicity of the biological simulation (four nitrogen-based compartments) enables a conceptually simple contrast between the simulated nitrogen budgets. Defining the organic nitrogen as that within the phytoplankton and detritus reservoirs, and the inorganic nitrogen as the nitrate and ammonium reserves, the total amount of organic nitrogen within the upper 10 m of northern MB increases by an average of

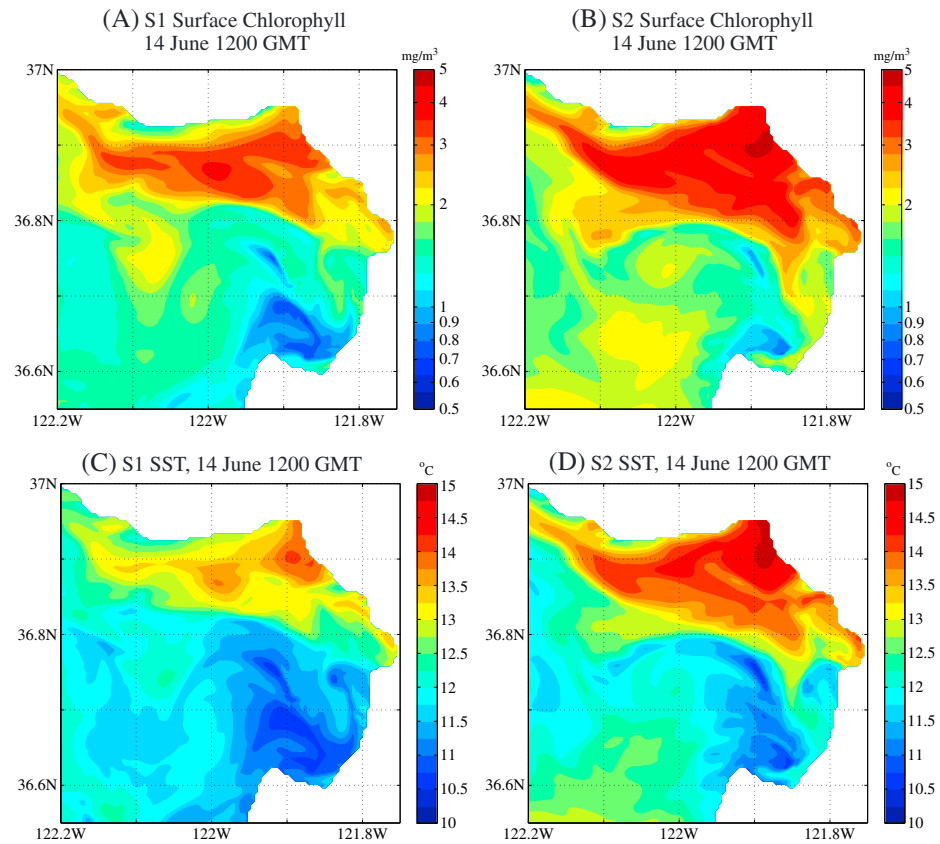


**Figure 9.** (a) S1 surface chlorophyll ( $\text{mg chl m}^{-3}$ ) on 14 June 1200 GMT; (b) the same for simulation S2. (c) SST for simulation S1 on 14 June 1200 GMT; (d) the same for S2.

10% in simulation S2 with a peak increase of 23% during the wind relaxation period (Figure 11). By the end of June, S2 has approximately 10% less inorganic N in the surface layer than S1 (Figure 11). The enhanced thermal stratification in S2 has a tendency to inhibit turbulent vertical diffusion, which would otherwise tend to homogenize the vertical distribution of scalar quantities. The additional biological benefit is that

phytoplankton are more restricted to the near-surface layer—sustaining continuing exposure to available light and improving the utilization of inorganic nitrogen for growth. This is particularly advantageous when light is more limiting to growth than available macronutrients.

Simultaneously, the increased thermal stratification in S2 restricts the egress of thermal energy out of the near-surface layer (< 10 m depth), and this also impacts the thermal energy budgets in addition to the nitrogen budgets. The respective diffusive differences tend to accelerate the rate of warming in S2 during periods wherein thermal stratification prevails in both simulations. For example, the S2 depth-averaged temperature in the upper 10.7 m from 12 June (2000 GMT) to 15 June (0600) in

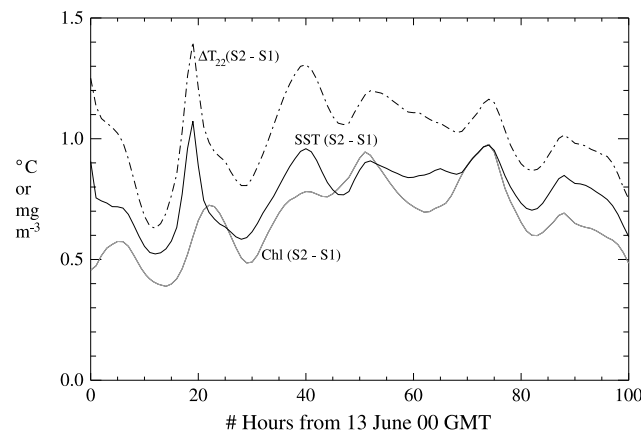


**Figure 10.** The hourly difference in mean SST ( $^{\circ}\text{C}$ ) for northern MB is depicted by the thick line. The difference in  $\Delta T_{22}$  ( $^{\circ}\text{C}$ ; an index of stratification, as explained in the text) is shown by the dashed line, and the chlorophyll difference ( $\text{mg m}^{-3}$ ) is shown by the gray line. In all cases, the difference is expressed as S2 – S1; positive differences indicate greater heat and biomass in the surface layers of simulation S2.

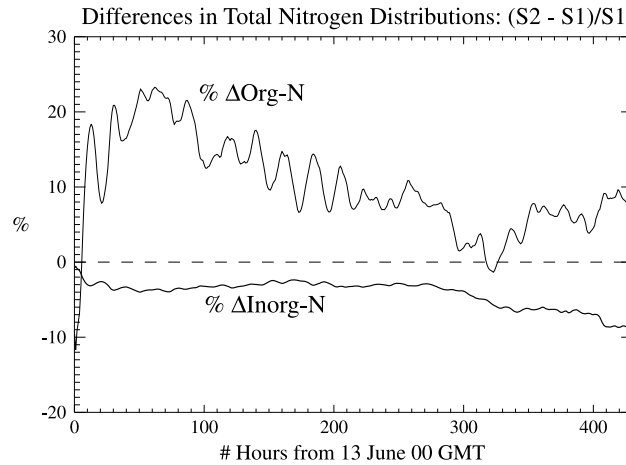


**Figure 11.** The thin line is the difference (as a %) between organic nitrogen (as defined in the text) in S2 versus S1 in the upper 10 m for northern MB. The total quantity of organic nitrogen in each simulation is used to calculate the difference as  $(S2 - S1)/S1 \times 100$ . The thick line is the inorganic nitrogen difference (as a %).

where  $Q_T$  is the total heat flux ( $W m^{-2}$ ) implied by the change in the upper layer temperature,  $Q_{sw}$  is the penetrating solar shortwave flux,  $R$  is the optical retention of solar shortwave at 10.7 m (or one minus the transmittance),  $Q_L$  is the latent heat flux,  $Q_S$  is the sensible heat flux,  $Q_{NL}$  is the net longwave ocean-atmosphere exchange, and finally  $Q_{vert}$  accounts largely for the vertical diffusion of heat out of the surface layer but may also include any vertical advective flux. The convention wherein fluxes out of the surface ocean layer are negative (a heat loss) is applied. Since the spatial means are taken from a large horizontal area ( $411 km^2$ ) in northern MB, horizontal advection and diffusion are dropped from the budget. The first four terms on the right-hand side (RHS) of equation (2) (the turbulent and radiative heat fluxes between the ocean and atmosphere; referred to herein as the “direct” fluxes) are recorded in the modeling system output at hourly intervals. The final RHS term, the diffusive flux out of the surface layer, is used as a closure term for the heat budget.

Accordingly, the direct fluxes during the above referenced period of warming for S2 average  $175.8 W m^{-2}$  (Table 1), and this implies a vertically diffusive heat removal ( $Q_{vert}$ ) of  $-57 W m^{-2}$ . In contrast, the same analysis for S1 yields a diffusive loss of  $-75 W m^{-2}$  (Table 1). Note that the main difference in the direct fluxes between S1 and S2 is due to the optical differences ( $R$ ). S1 relies on the Paulson and Simpson [1977] adaptation of the Jerlov IA oceanic water type: this yields an  $R$  value of 0.77 at 10.7 m. S2 relies on the biological model to determine the attenuation (biothermal feedback), and this  $R$  value at 10.7 m averages 0.95 during this period. Based strictly upon the differences in penetrating shortwave and allowing for the

northern MB increased at a rate of  $0.24^\circ C d^{-1}$ . Given the expression:

$$\frac{\Delta T}{\Delta t} = \frac{Q_T}{H\rho C_p} \quad (1)$$

where  $Q_T$  is the total heat flux ( $W m^{-2}$ ),  $H$  is the thickness of the water column (10.7 m),  $\rho$  is a reference seawater density, and  $C_p$  is the specific heat capacity for seawater, the increase in temperature per unit time implies a total heat flux into the surface layer of  $121.6 W m^{-2}$ . This S2 net heat flux and rate of temperature increase is approximately double that of S1 for the same time period (S1:  $0.12^\circ C d^{-1}$ ).

For each respective simulation, a total heat budget for the upper 10.7 m is given as

$$Q_T = Q_{sw}(R) + Q_L + Q_S + Q_{NL} + Q_{vert} \quad (2)$$

**Table 1.** S1 and S2 Heat Budgets: Term-by-Term Comparison

	S2	S1	(S2 - S1)
Net heating rate ( $^\circ C d^{-1}$ )	0.24	0.12	0.12
Net heat flux ( $Q_T$ ; $W m^{-2}$ )	121.6	60.8	60.8 <sup>a</sup>
Shortwave attenuation ( $R$ ) at 10.7 m	0.96	0.77	0.18
Attenuated shortwave ( $Q_{sw}(R)$ ; $W m^{-2}$ )	266.9	214.1	52.8
Latent heat flux ( $Q_L$ ; $W m^{-2}$ )	-18.0	-11.2	-6.8
Sensible heat flux ( $Q_S$ ; $W m^{-2}$ )	-1.7	-1.8	0.1
Longwave heat flux ( $Q_{NL}$ ; $W m^{-2}$ )	-71.4	-61.3	-10.1
Sum of direct fluxes ( $W m^{-2}$ )	175.8	139.8	36.0 <sup>b</sup>
Implied diffusive flux ( $Q_{vert}$ ; $W m^{-2}$ )	-54.2	-79.0	24.8 <sup>c</sup>
Heat flux below 10.7 m <sup>d</sup> ( $W m^{-2}$ )	65.3	142.9	-77.6

<sup>a</sup>Net heat flux difference.

<sup>b</sup>59.2 % of difference.

<sup>c</sup>40.8 % of difference.

<sup>d</sup>Convention is positive for heat penetration.

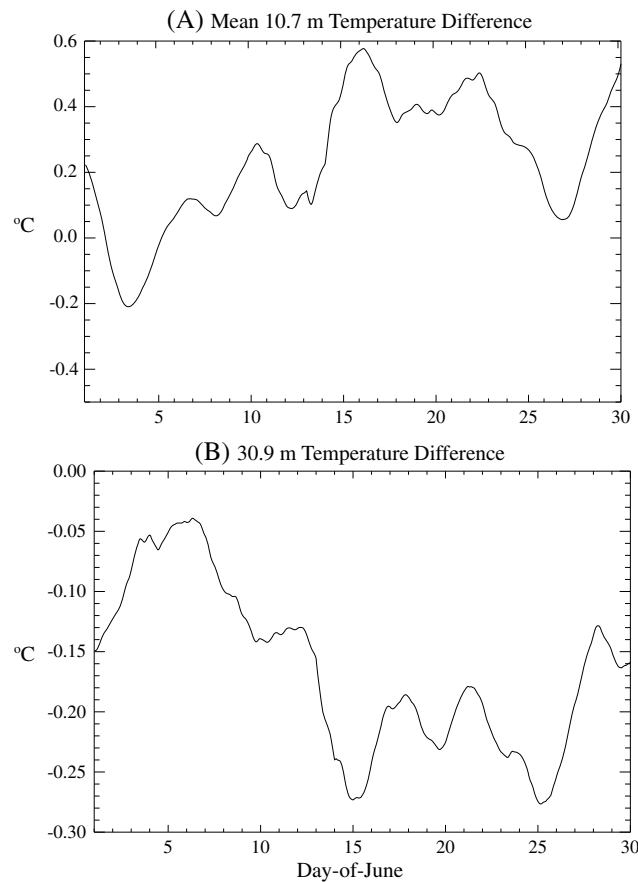


**Figure 12.** (a) Difference (S2 – S1) of the upper 10.7 m ocean temperature. (b) Difference (S2 – S1) of the respective ocean temperature at 30.9 m. All variables are extracted from the hourly model output increment and averaged over the spatial area of northern MB. The time series are smoothed with a 24 h moving average to remove high-frequency variability.

at the very beginning of the time series on 2 June and the dramatic lowering of the SST difference again on 27 June (Figures 5c and 12a). Another consequence of this apparent biothermal reorganization of thermal energy fluxes in the upper ocean is a simulated increase of the temporal SST variance: warming periods promote comparatively warmer SSTs, and mixing periods promote a comparatively more rapid SST cooling.

**4.3. Observations**

Are these simulated differences also seen in data? Since we are unable to replicate the numerical experiment in the “real world” by removing the bio-optical influence of phytoplankton from Monterey Bay, the focus of data analysis was instead placed on surface material property gradients and comparative intervariate relationships. Accordingly, the chlorophyll to temperature relationships as resolved by the simulations and recorded in the data were examined. Both of the simulations compare favorably to bottle Conductivity-Temperature-Depth (CTD) data (Figure 13) with respect to overall changes in chlorophyll magnitude and temperature increases; however, these discrete depth interval bottle data lack the vertical resolution necessary to determine if the differences in the respective simulations were also observed. Specifically, the upper 2.5 m of the water column in S2 resolve an additional ~0.2 units of normalized temperature increase ( $T_z/T_{50}$ ) that is not apparent in S1 (Figure 13b, blue shaded portion). Under the conditions of reduced winds, it is precisely this upper ocean difference in thermal stratification that is the main point of divergence between the two simulations.

Much finer vertical scale temperature data were obtained from the ScanFish towed platform (SF). This is a piloted vehicle that records data from an instrument suite as it transits from near surface to ~ 80 m depth

increase in S2 latent and longwave removal (due principally to a comparative increase in S2 SST), the S2 surface layer should warm at a rate exceeding that of S1 by only  $0.07^{\circ}\text{C d}^{-1}$ . However, the difference in apparent diffusive heat fluxes out of the surface layer increases this heating rate *difference* by 71% up to  $0.12^{\circ}\text{C d}^{-1}$ ; thus, the S2 surface layer is far more retentive than S1.

During June, S2 is biased warmer than S1 because periods favoring thermal stratification in the upper ocean are of longer duration than periods that promote turbulent vertical mixing. This tendency toward thermal stratification is typical of midlatitude coastal areas during the spring transition from winter well-mixed water column conditions to the characteristic thermal stratification of summer. However, note that during the mixing periods, S2 does indeed appear to lose heat at a faster rate than S1 (Figure 12a). Both the diffusive flux and the shortwave transmittance through 10.7 m are greater in S1 than in S2 (Table 1, last row). This difference introduces a cold bias in the subsurface waters of S2 (Figure 12b). Hence, when the water column does indeed overturn and turbulent forces prevail over the late spring and summer tendencies toward thermal stratification, colder waters mix into the surface layers of S2. This accounts for the reversal in sign for SST(S2 – S1) observed

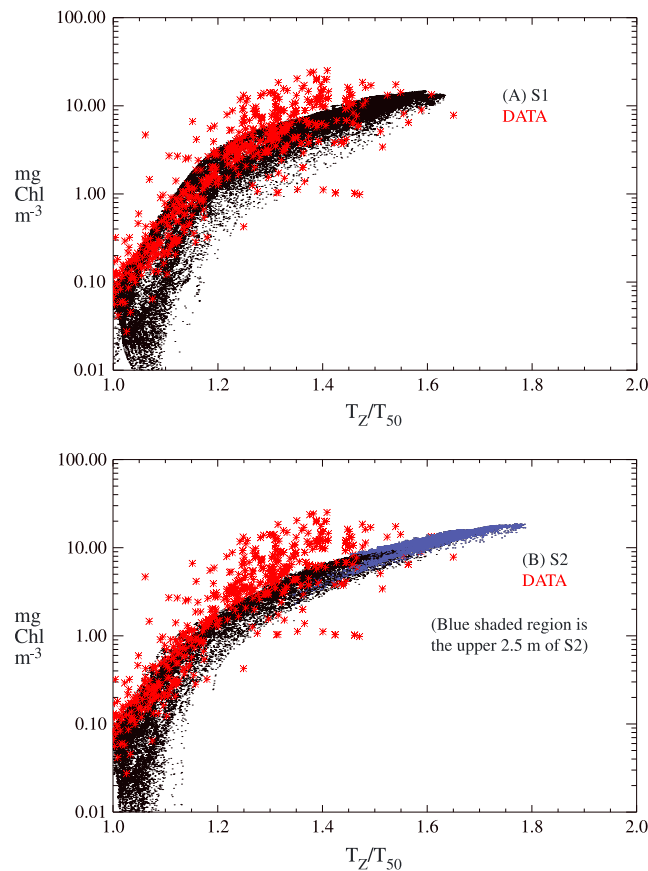


**Figure 13.** A comparison between simulated and observed (red asterisks) chlorophyll versus temperature relationships. The temperature is normalized by the temperature at 50 m depth ( $T_z/T_{50}$ ). Simulations (a) S1 and (b) S2; the in situ data are the same in both plots. The blue-shaded portion of Figure 13b is indicative of simulation data from the upper 2.5 m of the water column.

behind the ship. The data sampling resolution was roughly 2–3 observations per vertical meter [Jolliff *et al.*, 2012b]. An initial SF track was obtained during the onset of the mid-June wind relaxation event and over the northwest continental shelf between the 50 and 200 m isobaths (Figure 14a). Two profiles from the transect were extracted near the 50 m isobaths as prototypical examples of the temperature and optical profiles observed in northern Monterey Bay during the field study (Figures 14b and 14c). The temperature and the total absorption coefficient profiles ( $a_T(488)$ ) obtained from the AC-9 optical profiling instrument are highly correlated with one another. Continuous thermal stratification is evident from the surface down to a depth of ~22–25 m. In both observed profiles, intense near-surface (< 10 m) thermal gradients on the order of ~0.23°C per vertical meter are evident. The optical observations were used to calculate the trapping depth, i.e., the depth where ~95% of the total penetrating solar shortwave irradiance (~350–2500 nm) has been attenuated [Lee *et al.*, 2005] (see section A2 for calculation details). Due to the very high phytoplankton biomass in the surface layer (independently confirmed by High-Performance Liquid Chromatography

(HPLC) and fluorometer observations during the field study), the very high attenuation of the photosynthetically available radiation (PAR) spectral band (350–700 nm) shoals the total shortwave trapping depth to approximately 5 m in both observed profiles. For comparison, the depths where 95% of the more restricted PAR spectral band has been attenuated were also calculated: approximately 7.5 m for both observed profiles. The total shortwave attenuation is calculated as the sum of the infrared (IR) spectral band and the PAR spectral band. Attenuation of IR (> 700 nm) is largely invariant due to the absorption by pure seawater. PAR attenuation, in comparison, is severely impacted and increased by the presence of near-surface phytoplankton.

The observed temperature data were used to estimate the nitrate concentration profiles ( $^*NO_3$ ) using the linear temperature-to-nitrate relationship observed during the June 2008 MB field study. Nitrate consumption in the surface layer is thus inferred from the temperature gradient as well as the sharp increase in  $a_T(488)$ . Whereas the SF did not measure phytoplankton biomass directly, a separate analysis suggests that bulk changes in visible absorption coefficients in this system are primarily driven by changes in the concentration of phytoplankton pigments [Jolliff *et al.*, 2012b].

Simulated profiles for temperature, nitrate, and phytoplankton biomass were extracted from the spatiotemporally corresponding simulation results (Figures 14d and 14e). The sharp near-surface gradients in observed temperature are not replicated by S1 (Figure 13d). Instead, a much more gradual temperature gradient is simulated from ~10 to 30 m depth. The simulated phytoplankton biomass and nitrate profiles correspond to the more gradual density stratification. It is important to note the inappropriate discrepancy between the 95% PAR attenuation level and the trapping depth (Figure 14d). The former is a function of the simulated bio-optical attenuation, whereas the latter, serving as a direct input to the physical heating rate

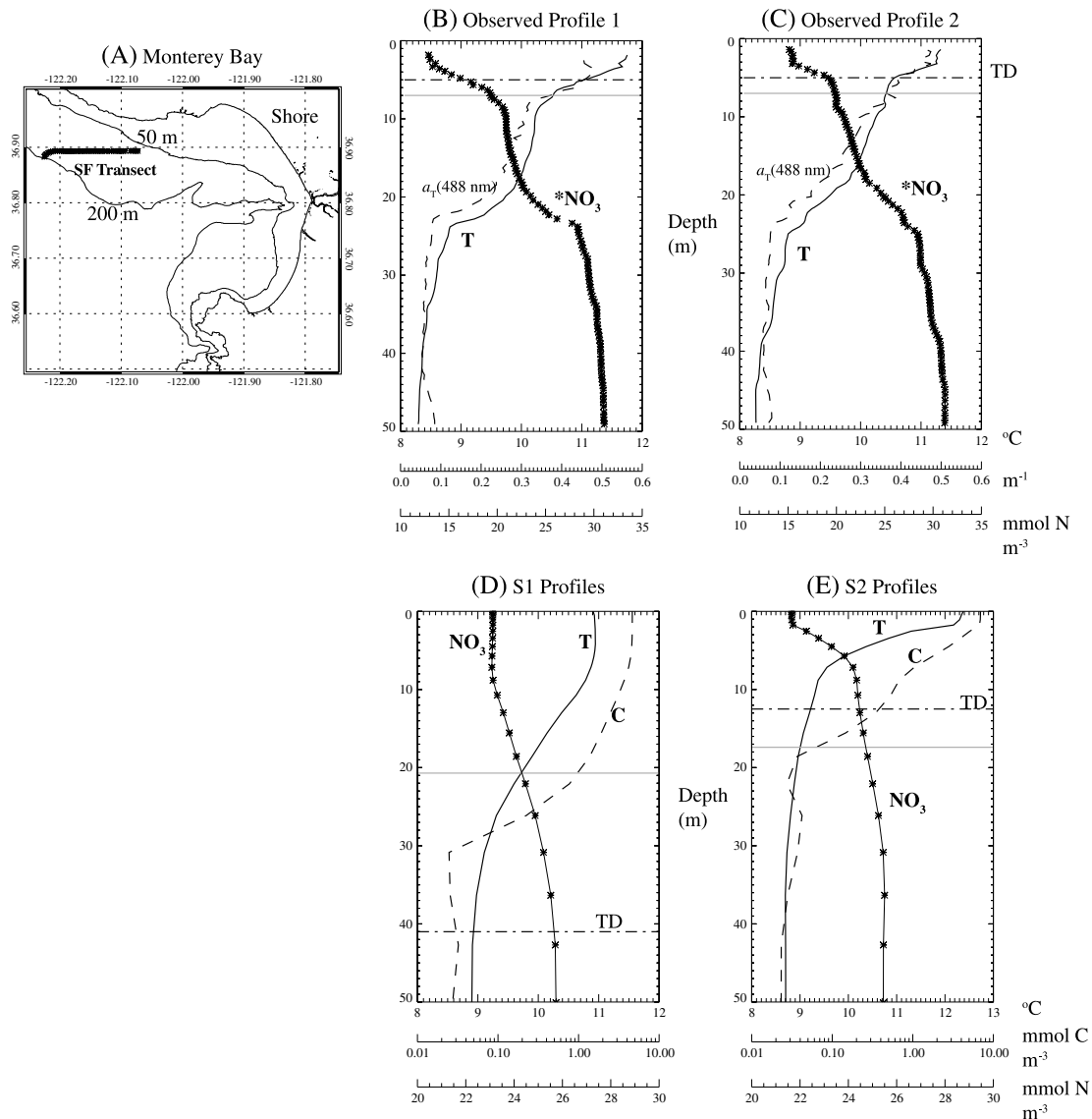


**Figure 14.** (a) Map of Monterey Bay with ScanFish transect from 50 to 200 m isobaths indicated; (b) observed profile of temperature, estimated nitrate, and optical absorption from the SF transect near the 50 m isobaths. The dot-dashed horizontal line is the estimated trapping depth; the thin gray line is the depth of 95% PAR attenuation. (c) As in Figure 14b for the adjacent profile. (d) The S1 simulated profiles of temperature, nitrate, and phytoplankton biomass, and (e) as in Figure 14d for S2.

computations of the ocean circulation model, is instead prescribed by the default attenuation values of the *Paulson and Simpson* [1977] scheme. These prescribed values force the trapping depth in S1 to be invariably located at 41 m. This is grossly in error when compared to the estimates derived from the optical observations. As a result, S1 fails to reproduce the sharp temperature (and other property) gradients observed in the upper 10 m of the water column.

In contrast, the upper 10 m fine structure of ocean temperature in S2 is closer to the observations (Figure 14e). The S2 trapping depth is within 8 m of the observed value (Figures 14d). This biologically enhanced optical attenuation is then directly communicated to the physical model that subsequently renders an S2 temperature gradient more consistent with the observations ( $> 0.2 \text{ } ^\circ\text{C m}^{-1}$ ). In both simulations, nitrate is above  $20 \text{ mmol N m}^{-3}$  and is thus not considered limiting to phytoplankton growth in the biological model (see section A1, equation (A5)). PAR penetration in both simulations, in comparison, is largely restricted to the upper 20 m of the water column. Thus, the additional vertical stability within the S2 surface layer, evidenced by the thermal gradient, facilitates an increased consumption of surface nitrate and a corresponding increase in near-surface phytoplankton biomass.

These simulated profile differences underscore the model result contrasts analyzed in previous sections. However, herein it is shown that S2 is more successful at reproducing the observed near-surface gradients and trends in temperature, nitrate, and potentially phytoplankton biomass, insofar as the optical observations may serve as a biomass proxy. The combined observations and simulations suggest that light availability, rather than macronutrient concentration, is the main constraint upon phytoplankton growth within this regime. Hence, the vertically stabilizing effect of biothermal feedback tends to concentrate phytoplankton biomass near the surface where nutrients may be utilized for growth more efficiently. This mechanism, in turn, shoals the trapping depth nearer the surface.

## 5. Discussion and Conclusions

*Ramp et al.* [1991] observed that under conditions of low wind stress and high solar insolation in coastal California, large vertical gradients in upper ocean temperatures occurred in patches consistent with high values of surface chlorophyll. They suggest that on the basis of their observations and simple one-dimensional heating rate calculations, it is the additional optical attenuation provided by surface phytoplankton stocks that brings about the observed surface heating and associated temperature gradient. The results presented here and in earlier work [Jolliff *et al.*, 2012a] support this hypothesis. However, here it is shown that the additional optical attenuation may not simply impact the vertical temperature structure and then cease to have any further impact; rather, the vertical temperature structure then feeds back to the biology to concentrate biomass near the surface and improve the nutrient utilization for growth. To use an engineering frame of reference, this is an example of a positive feedback loop.

The observations of *Ramp et al.* [1991] indicate that this biophysical feedback loop may reach extremes we are unable to presently simulate with our model: a 4.7°C gradient in the upper 2 m of ocean. Such fine-scale gradients are below the vertical grid scale of many ocean models. Nevertheless, our two-way coupled ocean-atmosphere simulations strongly suggest that such situations would have a profound impact on air-sea exchange of thermal energy and potentially many other upper ocean biological and physical processes. For example, an enhanced near-surface stratification and associated reduction in vertical diffusion may have important consequences for air-sea gas exchange that may impact carbon and oxygen budgets.

Vertical diffusion of ocean scalar quantities in this modeling system is quantified via the Mellor Yamada 2.5 vertical turbulence closure scheme [Mellor and Yamada, 1982]. This numerical recipe is one approximation out of many other possible choices [e.g., Large *et al.*, 1994]. Any numerical approximation for vertical mixing of scalars is likely to be imperfect. Nevertheless, the observations of *Ramp et al.* [1991] support the hypothesis that under the conditions of low wind stress and high solar insolation, surface phytoplankton blooms provide a biothermal feedback effect that may suppress vertical diffusion of thermal energy and other material properties. In the particular circumstance of Monterey Bay, California during the upwelling season, such increases in vertical stability are beneficial to the flora due to the relative abundance of macronutrients and the overall instability of this highly turbulent hydrodynamic regime.

The concept of flora having an impact on the physical environment that, in turn, further promotes the growth of the flora is analogous to the concept of “microclimates” in terrestrial vegetation. The most obvious example is the shading effect of a forest canopy: reducing incident PAR to sublethal levels, increasing moisture retention, and reducing temperatures and respiration costs [Callaway and Pugnaire, 2007, and references therein]. All of these effects are a perceived benefit to many species of vegetation emerging on the forest floor. Discovering a marine analogue of this situation for phytoplankton may at first seem dubious. The phytoplankton are, to first order, subject to the comparatively extreme physical disturbance and energy fluctuations of the surface ocean and are little more than passive recipients of whatever physical conditions may exist there. However, the evidence presented here and elsewhere shows that under some specific local conditions of reduced wind stress, high solar insolation, and available macronutrients, the optical properties of phytoplankton may indeed create a beneficial “microclimate” of vertical stability in the upper ocean (< 10 m depth) that promotes the growth and persistence of a surface phytoplankton bloom (> 2 mg m<sup>-3</sup> surface chlorophyll).

This biothermal potential of phytoplankton must also be considered with respect to diurnal warming. The diurnal thermocline and features of vertical stratification may be exploited by phytoplankton if sufficient nutrients are available. In a separate study, Jolliff *et al.* [2012b] examined the apparent fluorescence efficiency of phytoplankton from collocated fluorescence and optical data. The persistent surface warm layer near the

coasts within Monterey Bay was certainly exploited by diatoms (identified there by HPLC data) growing at eutrophic concentrations ( $>2 \text{ mg chl m}^{-3}$ ). Away from the coasts, however, the apparent fluorescence efficiency within an obviously diurnal surface warm layer suggested an impairment of the photosynthetic apparatus near the surface and chlorophyll observations there were generally below  $\sim 2 \text{ mg m}^{-3}$ . It was hypothesized that the availability of dissolved iron may impact the ability of phytoplankton in general, and diatoms in particular, to adapt to high-light conditions or highly variable light conditions near the air-sea interface and thus exploit the diurnal warm layer. The biological model integrated into COAMPS herein did not consider dissolved iron as a limiting nutrient or explicit state variable. Future work may have to consider iron dynamics more explicitly, or other biogeochemical processes that impact phytoplankton growth efficiency.

In conclusion, as integrated model simulations of the ocean-atmosphere system move toward finer scales of spatial and temporal resolution, investigators will need to consider the role of the biosphere in the ocean-atmosphere exchanges of energy and all of the processes subsequently impacted by this exchange. More broadly, the practice of modeling ocean physics independently of ocean biology and vice versa may have to cease. The situation is similar to that of meteorology and physical oceanography: one system (the ocean) cannot simply be prescribed as an invariant boundary condition to the other (the atmosphere). Instead, the dynamical interactions between the atmosphere and hydrosphere must be accounted for within the simulation itself. Our results strongly suggest that simulations of the upper ocean temperature structure, ocean-atmosphere exchange of thermal energy, and some aspects of the wind field and surface ocean circulation are dynamically sensitive to biothermal effects, and so the potential dynamical influence of the biosphere must also be considered.

## Appendix A: Model Formulae

### A1. Biological Model

The biological model integrated into COAMPS is a four-component nutrient-phytoplankton-detritus (NPD) model. Nitrate is initialized from observed temperature-to-nitrate relationships [Chavez *et al.*, 1996], and subsequent nitrogen cycling is allowed to “spin-up” as the simulated phytoplankton biomass assimilates nitrogen and is then subject to implicit grazing/mortality terms. Nitrogen-containing particulate detritus sinks and is subject to respiration. Mortality and respiration contribute to the ammonium pool, and the cycle is completed via light-inhibited nitrification. There is presently no benthic component in the model; particulate detritus that reaches the bottommost grid cell is respired back to the ammonium pool. Conversion between phytoplankton carbon and nitrogen is accomplished via the Redfield ratio [Redfield *et al.*, 1963].

The conservation equation for phytoplankton carbon ( $C$ ,  $\text{mmol C m}^{-3}$ ) follows the NCOM conservation equation for temperature given in Barron *et al.* [2006]:

$$\frac{\partial C}{\partial t} = -\nabla \cdot (VC) + A_H \nabla_H^2 C + \frac{\partial}{\partial z} \left( K_H \frac{\partial C}{\partial z} \right) + F(C) \quad (\text{A1})$$

Advection (first term on the right-hand side (RHS)), horizontal diffusion (second term on RHS), and vertical diffusion (third term on RHS) are solved via NCOM. The last term on the RHS represents the biological sources and sinks that are described in detail herein. Equation (A1) is applicable to the other three biological model state variables that are quantified with respect to nitrogen: nitrate ( $N_i$ ,  $\text{mmol N m}^{-3}$ ), ammonium ( $N_A$ ,  $\text{mmol N m}^{-3}$ ), and particulate detritus ( $D$ ,  $\text{mmol N m}^{-3}$ ). A complete list of parameters, state variables, and internal variables for the biological model is given in Table A1. The internal biological model time step ( $\Delta t$ ) is 5 s. Each state variable is defined over the entire three-dimensional coordinate domain ( $x, y, z$ ). Below, these spatial subscripts are dropped for simplicity, except where required to indicate depth ( $z$ ).

Phytoplankton growth is a function of available light and nitrogen. Light is quantified as downwelling photosynthetically available radiation ( $E_{PAR}$ ,  $\text{W m}^{-2}$ ). Description of the light attenuation is provided in section A2 as part of the optical computations. Expanding here the last term on the RHS of equation (A1):

$$F(C) = \frac{\Delta C}{\Delta t} = (\mu_r - \Gamma_r)C \quad (\text{A2})$$

The realized rate of growth ( $\mu_r$ ) is the minimum of the light-limited ( $\mu_L$ ) and nitrogen-limited ( $\mu_N$ ) growth rate calculations:

**Table A1.** Biological Model Parameters, State Variables, and Internal Variables

Parameter	Description	Units	Value
$Q_N$	Nitrogen half-saturation constant	$\text{mmol N m}^{-3}$	1.0
$\mu_{\max}$	Maximum phytoplankton growth rate	$\text{s}^{-1}$	$3.2 \times 10^{-5}$
$I_v$	Ivlev grazing parameter	$(\text{mmol C m}^{-3})^{-1}$	5.56
$\Gamma_{\max}$	Maximum phytoplankton grazing rate	$\text{s}^{-1}$	$5.8 \times 10^{-6}$
$S_1$	PAR saturation constant	$\text{W m}^{-2}$	145
$B_m$	Basal mortality rate	$\text{s}^{-1}$	$1.2 \times 10^{-6}$
$\varphi_1$	Grazing fraction-to-detritus pool	—	0.50
$\chi$	Molar nitrogen-to-carbon ratio	$\text{mol mol}^{-1}$	0.1509
$w_s$	Detritus sinking rate	$\text{m s}^{-1}$	$2.3 \times 10^{-4}$
$R_1$	Detritus loss rate	$\text{s}^{-1}$	$2.3 \times 10^{-6}$
$Q_{\text{ni}}$	Nitrification half-saturation constant	$\text{mmol N m}^{-3}$	1.0
$R_2$	Maximum nitrification rate	$\text{s}^{-1}$	$8.2 \times 10^{-5}$
$C_t$	C threshold concentration	$\text{mmol C m}^{-3}$	$1.0 \times 10^{-4}$
State variable			
$C$	Phytoplankton carbon	$\text{mmol C m}^{-3}$	
$N_I$	Nitrate (+nitrite)	$\text{mmol N m}^{-3}$	
$N_A$	Ammonium	$\text{mmol N m}^{-3}$	
$D$	Particulate detritus	$\text{mmol N m}^{-3}$	
Internal variable			
$\mu_r$	Realized phytoplankton growth rate	$\text{s}^{-1}$	
$\mu_L$	Light-limited phytoplankton growth rate	$\text{s}^{-1}$	
$\mu_N$	Nitrogen-limited phytoplankton growth rate	$\text{s}^{-1}$	
$\Gamma_r$	Realized phytoplankton loss rate	$\text{s}^{-1}$	
$N_T$	dissolved inorganic nitrogen	$\text{mmol N m}^{-3}$	
$N_A^*$	$N_A$ removal flux via nitrification	$\text{mmol N m}^{-3} \text{s}^{-1}$	

$$\mu_r = \text{MIN}(\mu_L, \mu_N) \quad (\text{A3})$$

where the light-limited growth rate is a function of  $E_{\text{PAR}}$  calculated for vertical level ( $z$ ), the PAR saturation constant ( $S_1$ ), and the maximum growth rate ( $\mu_{\max}$ , Table A1) [cf. Webb *et al.*, 1974]:

$$\mu_L = \mu_{\text{MAX}} \left( 1 - e^{-[E_{\text{PAR}}(S_1)^{-1}]} \right) \quad (\text{A4})$$

Nitrogen limitation is a function of the total nitrogen available ( $N_T = N_I + N_A$ ):

$$\mu_N = \mu_{\text{MAX}} \frac{N_T}{(N_T + Q_N)} \quad (\text{A5})$$

The realized rate of grazing is based on the Ivlev formulation [Ivlev, 1955; Hallam, 1978; Franks *et al.*, 1986] and requires a maximum potential rate ( $\Gamma_m$ ) and an Ivlev parameter ( $I_v$ ). The herbivore grazing rate saturates toward the maximum rate at elevated phytoplankton biomass ( $C$ ). Here a basal mortality rate ( $B_m$ ) is added to the expression:

$$\Gamma_r = \Gamma_m (1 - e^{-I_v C}) + B_m \quad (\text{A6})$$

If the phytoplankton carbon falls below a threshold value ( $C_t$ ) then  $\Gamma_r$  is set to 0.

Total grazing and mortality of phytoplankton biomass provides a source to the remaining nitrogen compartments. The biological terms for particulate detritus ( $D$ ) are given as follows:

$$F(D) = \frac{\Delta D}{\Delta t} = \Gamma_r C \chi f_1 - w_s \left( \frac{\Delta D}{\Delta z} \right) - R_1 D \quad (\text{A7})$$

where the grazed phytoplankton carbon is converted to nitrogen ( $\chi$ ) and multiplied by the fraction of grazed nitrogen allotted to the  $D$  pool ( $\varphi_1$ ). Sinking is calculated from the sinking speed parameter ( $w_s$ ) and the vertical detritus gradient. The loss rate ( $R_1$ ) represents the implicit bacterial respiration back to the ammonium compartment ( $N_A$ ). If the depth ( $z$ ) is at the maximum depth increment then  $D(z)$  is returned to the  $N_A(z)$  pool.

**Table A2.** Optical Model Parameters

Symbol	Description	Units	Value
$\theta$	Carbon-to-chlorophyll ratio (mass)	$\text{g g}^{-1}$	47.2
$\alpha_1$	Empirical absorption model coefficient 1	—	-0.017
$\alpha_2$	Empirical absorption model coefficient 2	—	0.076
$\alpha_3$	Empirical absorption model coefficient 3	—	0.554
$\alpha_4$	Empirical absorption model coefficient 4	—	-1.149
$\beta_1$	Empirical scattering model coefficient 1	—	0.416
$\beta_2$	Empirical scattering model coefficient 2	—	0.766
$b_{\text{bw}}(490)$	Pure seawater backscattering coefficient	$\text{m}^{-1}$	0.0012
$f_2$	Fraction of shortwave in PAR spectrum	—	0.48
$\varepsilon_1$	$K_1$ PAR attenuation coefficient 1	$\text{m}^{-1}$	-0.057
$\varepsilon_2$	$K_1$ PAR attenuation coefficient 2	—	0.482
$\varepsilon_3$	$K_1$ PAR attenuation coefficient 3	—	4.221
$\zeta_1$	$K_2$ PAR attenuation coefficient 1	$\text{m}^{-1}$	0.183
$\zeta_2$	$K_2$ PAR attenuation coefficient 2	—	0.702
$\zeta_3$	$K_2$ PAR attenuation coefficient 3	—	-2.567

Accordingly, the ammonium ( $N_A$ ) biological terms are given as follows:

$$\frac{\Delta N_A}{\Delta t} = \Gamma_r C_X (1 - f_1) + R_1 D - \mu_r C_X \frac{N_A}{N_T} - N_A^* \quad (\text{A8})$$

where the last term on the RHS ( $N_A^*$ ) is the ammonium mass flux lost to nitrification:

$$N_A^* = N_A \left( \frac{N_A}{N_A + Q_{\text{ni}}} \right) R_2 \quad (\text{A9})$$

Nitrification is only simulated in darkness: if  $E_{\text{PAR}}(z) > 0$ , then  $N_A^*(z) = 0$ .

The model does not distinguish nitrate versus nitrite oxidation states; thus, the nitrate state variable's biological terms ( $N_I$  = nitrate + nitrite) are given as follows:

$$\frac{\Delta N_I}{\Delta t} = N_A^* - \mu_r C_X \frac{N_I}{N_T} \quad (\text{A10})$$

$N_I$  is initialized from empirical temperature-to-nitrate relationships, and this is maintained at the model domain's boundary value points.

At 4 components and 13 parameters, this biological model is intended to present a minimal level of ecosystem and biogeochemical complexity. Phytoplankton functional groups, explicit zooplankton biomass, other nutrient sources/requirements, dissolved nonliving organic matter, a benthic component, and an explicit microbial loop are all omitted from this initial formulation. This model provides a framework wherein these additional terms and sets of equations may be added, as required, to improve model performance.

## A2. Optical Computations

Biological feedback to the physics is represented in the system via the variable penetration of solar shortwave energy into the surface ocean that is based upon the optical attenuation estimated in the biological model. This interface between the biological and physical ocean models replaces the "Jerlov" water types [Jerlov, 1976] previously used in the NCOM heating rate computations [Jolliff *et al.*, 2012a]. The attenuation of solar shortwave in the PAR spectral range (350–700 nm) is calculated identically in the physical and biological model components. This calculation is based upon Lee *et al.* [2005]. This method requires an estimate of the surface total absorption coefficient at 490 nm [ $a_T(490)$ ] and the total surface backscattering coefficient at 490 nm [ $b_{\text{bT}}(490)$ ]. These quantities are calculated from the surface phytoplankton carbon (C) biological state variable as follows:

$$\log_{10}[a_T(490)] = \alpha_1 \text{clog}3 + \alpha_2 \text{clog}2 + \alpha_3 \text{clog} + \alpha_4 \quad (\text{A11})$$

and

$$\text{clog} = \log_{10}(C^* \theta^{-1}) \quad (\text{A12})$$

where  $C^*$  is the phytoplankton carbon in mass units ( $\text{mg C m}^{-3}$ ) and  $\theta$  is the carbon-to-chlorophyll mass ratio (Table A2). All optical coefficient values are given in Table A2. Equation (A11) is an empirical relationship

between phytoplankton chlorophyll and total absorption coefficients obtained from in situ data from Monterey Bay [Jolliff *et al.*, 2012b]. The carbon-to-chlorophyll ratio value (Table A2) is also obtained from these data. This empirical expression implicitly includes the absorption signal that may arise from nonliving organic matter associated with phytoplankton productivity.

The calculation of the total backscattering coefficient [ $b_{bT}(490)$ ] is based on literature. The particle scattering coefficient at 550 nm [ $b_p(550)$ ] as a function of chlorophyll concentration is taken from Morel and Maritorena [2001]:

$$[b_p(550)] = \beta_1 (C^* \theta^{-1})^{\beta_2} \quad (A13)$$

The total backscattering coefficient at 490 nm is calculated as a function of  $b_p(550)$ :

$$[b_{bT}(490)] = \left\{ 0.002 + 0.01[0.50 - 0.25(\text{clog})] \left( \frac{490}{550} \right)^v \right\} [b_p(550)] + b_{bw}(490) \quad (A14)$$

where

$$v = (0.5)(\text{clog} - 0.3), \quad 0.02 < [C^* \theta^{-1}] < 2 \text{ mg m}^{-3} \quad (A15)$$

and

$$v = 0, \quad [C^* \theta^{-1}] > 2 \text{ mg m}^{-3} \quad (A16)$$

Once these optical quantities are determined [ $a_T(490)$ ,  $b_{bT}(490)$ ], the Lee *et al.* [2005] algorithm is employed to attenuate simulated shortwave into the surface ocean. Total shortwave ( $E_T$ ,  $\text{W m}^{-2}$ ) just below the air-sea interface ( $z=0^-$ ) is partitioned into PAR ( $E_{PAR}$ ,  $\text{W m}^{-2}$ ) and infrared ( $E_{IR}$ ,  $\text{W m}^{-2}$ ) spectral components. This follows the Lee *et al.* [2005] spectral partition for PAR (350–700 nm) and IR (700–2500 nm).

$$E_{PAR}(0^-) = E_{TOT}(0^-) f_2, \quad E_{IR}(0^-) = E_{TOT}(0^-) (1 - f_2) \quad (A17)$$

It is assumed that 48% of the total shortwave is in the PAR spectral range (Table A2). The attenuation coefficients for PAR ( $K_{PAR}(z)$ ) and IR ( $K_{IR}(z)$ ) are both a function of depth:

$$E_{PAR}(z) = E_{PAR}(0^-) e^{-K_{PAR}(z)z} \quad (A18)$$

and

$$E_{IR}(z) = E_{IR}(0^-) e^{-K_{IR}(z)z} \quad (A19)$$

The depth-dependent attenuation coefficient for IR ( $K_{IR}(z)$ ) is

$$K_{IR}(z) = 0.56 + \frac{2.304}{(0.001 + z)^{0.65}} \quad (A20)$$

PAR attenuation is also from Lee *et al.* [2005] but requires several additional computation steps:

$$K_{PAR}(z) = K_1 + \frac{K_2}{(1.0 + z)^{0.5}} \quad (A21)$$

where

$$K_1 = \varepsilon_1 + \varepsilon_2 [a_T(490)]^{0.5} + \varepsilon_3 [b_{bT}(490)] \quad (A22)$$

and

$$K_2 = \zeta_1 + \zeta_2 [a_T(490)] + \zeta_3 [b_{bT}(490)] \quad (A23)$$

The attenuation of  $E_{IR}$  and  $E_{PAR}$  are required for the NCOM heating rate computations. The incident total shortwave is simulated via the COAMPS atmospheric model component. The attenuation of  $E_{PAR}$  is also required for the biological model: the value of PAR at each vertical level ( $z$ ) is used in equation (A4) to determine the light-limited rate of growth.

It is important to note that given the above equations, the phytoplankton biomass state variable is the driver of changes in the total absorption and total backscattering coefficients, and the subsequent alterations to  $K_{PAR}(z)$ . This Case 1-type assumption [Morel and Prieur, 1977] is appropriate for Monterey Bay, California,

and other marine environments wherein phytoplankton and associated nonliving organic matter are the dominant bio-optical constituents. Two important points need to be clarified with respect to the biological and optical formulations presented herein. First, we recognize and caution that other processes such as terrestrial runoff, dispersion of river plumes, and suspension of mineral sediments (i.e., Case 2) would violate our optical assumptions. These additional processes will be addressed in future work by the addition of terms to the state variable space and associated optical terms to equations (A11) and (A14).

Second, the sinking mass of organic detritus represented explicitly in our biological state variable space ( $D$ , equation (A7)) is not represented by a specific mass to optical property mathematical transform in our optical equations. Instead, equations (A11) and (A14) use the Case 1 assumption to render the total absorption and backscattering coefficients as an empirical function of the phytoplankton biomass. In the case of absorption coefficients, this is because the main contributor from nonliving organic matter is due to colored detrital matter, or CDM [see Siegel *et al.*, 2005], which includes a largely dissolved component. These materials are generally refractory, depleted in nitrogen [Kahler and Koeve, 2001], and require additional sets of state variables and parameterizations than those presented within our simple NPD model framework. Future work will move toward more explicit representations of CDM in both the biological and optical model equations.

#### Acknowledgments

This work was supported by the Naval Research Laboratory 6.2 project "Resolving Bio-Optical Feedbacks to Ocean/Atmosphere Dynamics" and the NRL 6.1 project "Buoyancy Plume Modulation of Coastal Air-Sea Exchange Processes." The authors thank Stephanie Anderson for help preparing figures. The authors also thank anonymous reviewers and Shubha Sathyendranath for comments that improved the manuscript. The wind data presented in Figure 4a were provided by the Monterey Bay Aquarium Research Institute ([www.mbari.org](http://www.mbari.org)).

#### References

- Anderson, W. G., A. Gnanadesikan, R. Hallberg, J. Dunne, and B. Samuels (2007), Impact of ocean color on the maintenance of the Pacific Cold Tongue, *Geophys. Res. Lett.*, *34*, L11609, doi:10.1029/2007GL030100.
- Bannister, T. T., and A. D. Weidemann (1984), The maximum quantum yield of phytoplankton photosynthesis *in situ*, *J. Plankton Res.*, *6*, 275–294.
- Barron, C. N., A. B. Kara, H. E. Hurlburt, C. Rowley, and L. F. Smedstad (2004), Sea surface height predictions from the Global Navy Coastal Ocean Model (NCOM) during 1998–2001, *J. Atmos. Oceanic Technol.*, *21*, 1876–1894.
- Barron, C. N., A. B. Kara, P. J. Martin, R. C. Rhodes, and L. F. Smedstad (2006), Formulation, implementation and examination of vertical coordinate choices in the global Navy Coastal Ocean Model (NCOM), *Ocean Model.*, *11*, 347–375, doi:10.1016/j.ocemod.2005.01.004.
- Breaker, L., and W. Broenkow (1994), The circulation in Monterey Bay and related processes, *Oceanogr. Mar. Biol.*, *32*, 1–64.
- Bricaud, A., A. Morel, and L. Prieur (1981), Absorption by dissolved organic matter of the sea (yellow substance) in the UV and visible domains, *Limnol. Oceanogr.*, *26*(1), 43–53.
- Cahill, B., O. Schofield, R. Chant, J. Wilkin, E. Hunter, S. Glenn, and P. Bissett (2008), Dynamics of turbid buoyant plumes and the feedbacks on near-shore biogeochemistry and physics, *Geophys. Res. Lett.*, *35*, L10605, doi:10.1029/2008GL033595.
- Callaway, H. L., and F. I. Pugnaire (2007), Facilitation in plant communities in *Functional Plant Ecology*, 2nd ed., edited by F. Pugnaire and F. Valladares, 726 pp., CRC Press, Boca Raton, Fla.
- Chavez, F. P., and M. Messié (2009), A comparison of Eastern Boundary Upwelling Ecosystems, *Prog. Oceanogr.*, *83*(1–4), 80–96, doi:10.1016/j.pocean.2009.07.032.
- Chavez, F. P., S. K. Service, and S. E. Buttery (1996), Temperature-nitrate relationships in the central and eastern tropical Pacific, *J. Geophys. Res.*, *101*, 20,553–520,563, doi:10.1029/96JC01943.
- Cummings, J. A. (2005), Operational multivariate ocean data assimilation, *Q. J. R. Meteorol. Soc.*, *131*, 3582–3604.
- Doyle, J. D., Q. Jiang, Y. Chao, and J. Farrara (2009), High-resolution real-time modeling of the marine atmospheric boundary layer in support of the AOSN-II field campaign, *Deep Sea Res. Part II: Topical Studies in Oceanography*, *56*(3–5), 87–99, doi:10.1016/j.dsr2.2008.08.009.
- Eliassen, S. K., E. Gaard, B. Hansen, and K. M. H. Larsen (2005), A "horizontal Sverdrup mechanism" may control the spring bloom around small oceanic islands and over banks, *J. Mar. Syst.*, *56*(3–4), 352–362, doi:10.1016/j.jmarsys.2005.03.005.
- Fairall, C. W., E. F. Bradley, D. P. Rogers, J. B. Edson, and G. S. Young (1996), Bulk parameterization of air-sea fluxes for TOGA COARE, *J. Geophys. Res.*, *101*, 3747–3764, doi:10.1029/95JC03205.
- Falkowski, P. (1994), The role of phytoplankton photosynthesis in global biogeochemical cycles, *Photosynth. Res.*, *39*, 235–258.
- Franks, P. J. S., J. S. Wroblewski, and G. R. Flierl (1986), Behavior of a simple plankton model with food-level acclimation by herbivores, *Mar. Biol.*, *91*, 121–129.
- Graham, W. M., and J. L. Largier (1997), Upwelling shadows as nearshore retention sites: The example of northern Monterey Bay, *Cont. Shelf Res.*, *17*(5), 509–532.
- Hallam, T. G. (1978), Structural sensitivity of grazing formulations in nutrient controlled plankton models, *J. Math. Biol.*, *5*, 269–280.
- Hodur, R. M. (1997), The Naval Research Laboratory's Coupled Ocean/Atmosphere Mesoscale Prediction System (COAMPS), *Mon. Weather Rev.*, *125*(7), 1414–1430.
- Ivlev, V. S. (1955), *Experimental Ecology of the Feeding of Fishes*, 302 pp., Pischepromizdat, Moscow, Russia.
- Jerlov, N. G. (1976), *Marine Optics*, 231 pp, Elsevier Science, Amsterdam, Netherlands.
- Jolliff, J. K., T. A. Smith, C. N. Barron, S. Derada, S. C. Anderson, R. W. Gould, and R. A. Arnone (2012a), The impact of coastal phytoplankton blooms on ocean-atmosphere thermal energy exchange: Evidence from a two-way coupled numerical modeling system, *Geophys. Res. Lett.*, *39*, L24607, doi:10.1029/2012GL053634.
- Jolliff, J. K., R. W. Gould, Jr., B. Penta, W. J. Teague, S. DeRada, F. P. Chavez, and R. A. Arnone (2012b), Water mass bio-optical properties in the Monterey Bay region: Fluorescence-based inference of shifts in phytoplankton photophysiology, *J. Geophys. Res.*, *117*, C07019, doi:10.1029/2011JC007568.
- Kahler, P., and W. Koeve (2001), Marine dissolved organic matter: Can its C:N ratio explain carbon overconsumption?, *Deep Sea Res., Part I*, *48*, 49–62.
- Kara, A. B., H. E. Hurlburt, P. A. Rochford, and J. J. O'Brien (2004), The impact of water turbidity on interannual sea surface temperature simulations in a layered global ocean model, *J. Phys. Oceanogr.*, *34*, 345–359.

- Large, W. G., J. C. McWilliams, and S. C. Doney (1994), Oceanic vertical mixing: A review and a model with a nonlocal boundary layer parameterization, *Rev. Geophys.*, *32*(4), 363–403, doi:10.1029/94RG01872.
- Lee, Z., K. Du, R. A. Arnone, S. Liew, and B. Penta (2005), Penetration of solar radiation in the upper ocean: A numerical model for oceanic and coastal waters, *J. Geophys. Res.*, *110*, C09019, doi:10.1029/2004JC002780.
- Lewis, M. R., J. J. Cullen, and T. Platt (1983), Phytoplankton and thermal structure in the upper ocean: Consequences of nonuniformity in chlorophyll profile, *J. Geophys. Res.*, *88*, 2565–2570, doi:10.1029/JC088iC04p02565.
- Longhurst, A. (1998), *Ecological Geography of the Sea*, 398 pp., Academic Press, San Diego and London.
- Manizza, M., C. Le Quere, A. J. Watson, and E. T. Buitenhuis (2008), Ocean biogeochemical response to phytoplankton-light feedback in a global model, *J. Geophys. Res.*, *113*, C10010, doi:10.1029/2007JC004478.
- Mellor, G. L., and T. Yamada (1982), Development of a turbulence closure model for geophysical fluid problems, *Geophys. Res.*, *20*, 851–875.
- Morel, A. (1978), Available, usable, and stored radiant energy in relation to marine photosynthesis, *Deep-Sea Res.*, *25*, 673–688.
- Morel, A. (1988), Optical modeling of the upper ocean in relation to its biogenous matter content (case I waters), *J. Geophys. Res.*, *93*, 10,749–10,768, doi:10.1029/JC093iC09p10749.
- Morel, A., and D. Antoine (1994), Heating rate within the upper ocean in relation to its bio-optical state, *J. Phys. Oceanogr.*, *24*, 1652–1665.
- Morel, A., and S. Maritorena (2001), Bio-optical properties of oceanic waters: A reappraisal, *J. Geophys. Res.*, *106*, 7163–7180, doi:10.1029/2000JC000319.
- Morel, A., and L. Prieur (1977), Analysis of variation in ocean color, *Limnol. Oceanogr.*, *22*(4), 709–722.
- Oschlies, A. (2004), Feedbacks of biotically induced radiative heating on upper-ocean heat budget, circulation, and biological production in a coupled ecosystem-circulation model, *J. Geophys. Res.*, *109*, C12031, doi:10.1029/2004JC002430.
- Patara, L., M. Vichi, S. Masina, P. G. Fogli, and E. Manzini (2012), Global response to solar radiation absorbed by phytoplankton in a coupled climate model, *Clim. Dyn.*, *39*(7–8), 1951–1968.
- Paulson, C. A., and J. J. Simpson (1977), Irradiance measurements in the upper ocean, *J. Phys. Oceanogr.*, *7*, 952–956.
- Pennington, J. T., and F. P. Chavez (2000), Seasonal fluctuations of temperature, salinity, nitrate, chlorophyll and primary production at station H3/M1 over 1989–1996 in Monterey Bay, California, *Deep-Sea Research II*, *47*, 947–974.
- Ramp, S. R., R. W. Garwood, C. O. Davis, and R. L. Snow (1991), Surface heating and patchiness in the coastal ocean off central California during a wind relaxation event, *J. Geophys. Res.*, *96*, 14,947–14,957, doi:10.1029/91JC01140.
- Ramp, S. R., J. D. Paduan, I. Shulman, J. Kindle, F. L. Bahr, and F. Chavez (2005), Observations of upwelling and relaxation events in the northern Monterey Bay during August 2000, *J. Geophys. Res.*, *110*, C07013, doi:10.1029/2004JC002538.
- Redfield, A. C., B. H. Ketchum, and F. A. Richards (1963), The influence of organisms on the composition of seawater, in *The Sea*, Interscience, New York, NY, vol. 2, p. 26–77.
- Rochford, P. A., A. B. Kara, A. J. Wallcraft, and R. A. Arnone (2001), Importance of solar subsurface heating in ocean general circulation models, *J. Geophys. Res.*, *106*, 30,923–30,938, doi:10.1029/2000JC000355.
- Ryan, J. P., M. A. McManus, and J. M. Sullivan (2010), Interacting physical, chemical and biological forcing of phytoplankton thin-layer variability in Monterey Bay, California, *Cont. Shelf Res.*, *30*(1), 7–16, doi:10.1016/j.csr.2009.10.017.
- Siegel, D. A., S. Maritorena, and N. B. Nelson (2005), Independence and interdependencies among global ocean color properties: Reassessing the bio-optical assumption, *J. Geophys. Res.*, *110*, C07011, doi:10.1029/2004JC002527.
- Small, R. J., S. Carniel, T. Campbell, J. Teixeira, and R. Allard (2012), The response of the Ligurian and Tyrrhenian Seas to a summer Mistral event: A coupled atmosphere–ocean approach, *Ocean Modell.*, *48*(0), 30–44, doi:10.1016/j.ocemod.2012.02.003.
- Sweeney, E. N., D. J. Jr. McGillicuddy, and K. O. Buesseler (2003), Biogeochemical impacts due to mesoscale eddy activity in the Sargasso Sea as measured at the Bermuda Atlantic Time-series Study (BATS), *Deep Sea Res., Part II*, *50*, 3017–3039.
- Walsh, J. J. (1988), *On the Nature of Continental Shelves*, Academic Press, San Diego, pp. 515.
- Webb, W. L., M. Newton, and D. Starr (1974), Carbon dioxide exchange of *Alnus rubra*, A mathematical model, *Oecologia Berl.*, *17*, 281–291.
- Wu, Y., C. C. L. Tang, S. Sathyendranath, and T. Platt (2007), The impact of bio-optical heating on the properties of the upper ocean: A sensitivity study using a 3-D circulation model for the Labrador Sea, *Deep-Sea Res. II*, *54*, 2630–2642.